

Observation of Robust and Coherent Non-Abelian Hadron Dynamics on Noisy Quantum Processors

Fran Ilčić^{1,*}, Ritajit Majumdar^{2,*}, Emil Mathew^{1,*}, Nathan Earnest-Noble³, & Indrakshi Raychowdhury¹

¹Department of Physics and Center for Research in Quantum Information and Technology,

Birla Institute of Technology and Science Pilani,

K K Birla Goa Campus, Zuarinagar, Sancole, Goa 403726, India.

²IBM Quantum, IBM India Research Lab, India.

³IBM Quantum, IBM T.J. Watson Research Center, Yorktown Heights, NY 10598, USA.

* contributed equally.

The real-time evolution of strongly interacting matter remains a frontier of fundamental physics, as classical simulations are hampered by exponential Hilbert space growth and entanglement-driven bottlenecks in tensor networks. This study reports the quantum simulation of hadron dynamics within a $(1+1)$ -dimensional $SU(2)$ lattice gauge theory using a 156-qubit IBM superconducting processor. Leveraging a hardware-efficient Loop-String-Hadron (LSH) encoding, we simulate the dynamics of the physical degrees of freedom on a 60-site lattice in the weak-coupling regime, as a crucial step toward the continuum limit. We successfully observe the light-cone propagation of a confined meson and internal oscillations indicative of early-time hadronic breathing modes. Notably, these high-fidelity results were obtained directly from the quantum data via a differential measurement protocol, together with measurement error mitigation, demonstrating a robust pathway for large-scale simulations even on noisy hardware. To validate the results, we benchmarked the quantum algorithm and outcome from the quantum processor against state-of-the-art approximated classical algorithms using CPU – based on tensor network methods and Pauli propagation methods respectively. Furthermore, we provide a quantitative comparison demonstrating that as the system approaches the weak-coupling or the continuum limit, the quantum processor maintains a consistent structural robustness where classical tensor networks and Pauli propagation methods encounter an onset of exponential complexity or symmetry violations as an artifact of approximation in the algorithm. These results establish a scalable pathway for simulating non-Abelian dynamics on near-term quantum hardware and mark a critical step toward achieving a practical quantum advantage in high-energy physics.

pute static properties, they cannot tackle real-time evolution due to the sign problem. Tensor Network (TN) methods offer a partial solution in low dimensions but hit a fundamental “entanglement wall” during quenches: as time evolves, the entanglement entropy $S(t)$ grows linearly, requiring the bond dimension to grow exponentially to maintain accuracy. This renders long-time simulations of large lattices computationally prohibitive for classical machines.

Quantum simulation, utilizing either digital gate-based or analog approaches, provides a fundamental route around this barrier by mapping gauge fields directly onto controllable quantum degrees of freedom. However, scalable experimental demonstrations have been predominantly confined to Abelian models, such as $U(1)$ or \mathbb{Z}_2 lattice gauge theories [1, 2, 3, 4, 5, 6, 7, 8, 9, 10, 11, 12, 13]. The transition to non-Abelian symmetries [14, 15, 16, 17, 18], a strictly necessary step for simulating $SU(3)$ and the phenomenology of Quantum Chromodynamics (QCD) [19, 20], remains stalled by the difficulty of enforcing non-commuting Gauss’s laws on physical hardware. While analog simulators often lack the flexibility to implement these complex local constraints, current digital quantum devices face a parallel challenge: the deep circuits required to enforce gauge invariance are typically overwhelmed by hardware noise. Accessing the dynamics over longer timescales and reaching the continuum, or even the thermodynamic limit, remained a long-term goal for the community.

In this work, we overcome these limitations by using the Loop-String-Hadron (LSH) framework [21], which restructures the local Hilbert space to enforce Gauss’s law without the non-local string operators that plague standard Jordan-Wigner encodings. With this hardware-efficient encoding approach, we are able to scale the simulation of the dynamics of a meson in $(1+1)$ -dimensional lattice gauge theory to a 60-staggered-site $SU(2)$ model using a 156-qubit superconducting processor—approaching the thermodynamic limit. The coupling constants are chosen to fall in the weak-coupling regime, where entanglement is expected to grow rapidly, while the quantum algorithm involves a constant circuit depth per time step. We simulate dynamics of the system with a noise-resilient measurement protocol [22]. By isolating the coherent signal through differential observation, we extract high-fidelity hadronic physics directly from the data, reducing the gap between small-scale proofs of principle and utility-scale quantum hardware.

State-of-the-art classical simulation of the quantum circuit, the Pauli Propagation method [23] as well as tensor network simulation of the physical system are performed to validate the quantum algorithm and experimental results. A separation in time scaling is observed between the quantum execution time with a fixed shot budget and measurement error mitigation, and execution of classical algorithms, suggesting a possible algorithmic benefit in obtaining time evolution data over a small time window. Probing deeper into the weak coupling domain revealed when both the tensor network and Pauli Propagation struggles

Gauge theories form the bedrock of the Standard Model, yet predicting their non-equilibrium dynamics remains notoriously difficult. While Euclidean Monte Carlo methods successfully com-

with entanglement barrier and growth of non-clifford ness. The quantum processor, on the other hand is not affected by any of these except hardware noise in the current era of pre-fault tolerant hardware. A potential benefit can thus be envisioned in quantum simulating the strong interaction of nature with fault tolerant device and current work paves the pathway.

The Physics and the Experiment

In this work, we focus on the simplest continuous, yet non-Abelian, gauge group $SU(2)$ in $(1+1)$ spacetime dimensions – with the ultimate aim of simulating the strong interactions of nature, described by $SU(3)$ gauge theory in $(3+1)$ dimensions. The system consists of dynamical fermions (matter) interacting via $SU(2)$ gauge fields defined on the links of a spatial lattice. Understanding the structure and dynamics of entanglement entropy provides a new tool in the era of quantum information science [24]. Although various dynamical phenomena have been envisaged in different model-building and phenomenological predictions [25, 26], the scientific community has been waiting for an ab initio calculation or a quantum simulation demonstrating its validity and revealing many quantum mechanisms underlying the existing effective or microscopic description of physics in out-of-equilibrium or in extreme environments.

The Hamiltonian and Its Continuum Limit

The dynamics of gauge fields coupled with staggered fermions are governed by the Kogut-Susskind Hamiltonian [27]. The Hamiltonian contains an electric energy term (H_E), a staggered mass term H_M and a matter gauge interaction term (H_I) combined as:

$$H = \frac{g^2}{2a} H_E + m H_M + \frac{1}{2a} H_I \quad (1)$$

The parameters g , m , and a denote the gauge coupling, lattice fermion mass, and lattice spacing, respectively. The central challenge in simulating high-energy physics is to recover the *continuum limit*, in which the lattice spacing $a \rightarrow 0$ and the discrete theory faithfully reproduces the continuous quantum field theory (QFT). In $(1+1)$ dimensions, this limit corresponds to the regime of vanishing coupling, $g \rightarrow 0$, provided the simulation volume is sufficiently large to capture the relevant physics. The volume of the system is given by $L = Na$, for an N -site system. The Hamiltonian given in (1) can be scaled as

$$W = \frac{2a}{g^2} H = H_E + \mu H_M + x H_I \quad (2)$$

The couplings in W with electric, mass and matter-gauge interaction terms are dimensionless and given as 1, μ , x respectively, where $x = \frac{1}{g^2 a^2}$ & $\mu = 2 \frac{m}{g} \sqrt{x}$. For a chosen fixed value of $\frac{m}{g}$, the continuum limit of the theory lies at $N \rightarrow \infty$ and $x \rightarrow \infty$ [28]. The work primarily focuses on $N = 60$ and $x = 100$, where the results from tensor network and Pauli propagation methods agree reasonably with the QPU result, with the chosen level of accuracy, and demonstrate runtime advantage for QPU for a fixed shot budget with measurement error mitigation only. We further study a lower and a higher value of x , to conclude that the struggle for classical simulations using tensor network or Pauli Propagation Method increases with increasing value of x , keeping N constant. This result is presented in Fig. 4.

Encoding Non-Abelian Gauge Invariance

A crucial hurdle in simulating the dynamics of a gauge theory arises from the need for gauge invariance. Although a gauge-invariant and orthonormal basis provides a natural choice for efficient encoding, commonly used basis – such as Wilson loops and strings – are inherently non-local. A further difficulty lies in expressing the Hamiltonian in terms of universal gate sets implementable on physical quantum hardware. When dealing with noise in today’s quantum hardware, locality can be crucial for maintaining gauge invariance throughout the dynamic simulation. To date, a scalable and immediately implementable algorithm for non-Abelian gauge theories has remained absent, even in the era of utility-scale quantum hardware [29].

The dynamics, governed by the Hamiltonian in (1), preserves gauge invariance generated by a set of three Gauss law operators $G^a(r)$ for $a = 1, 2, 3$ and $\forall r$. These generators satisfy the $SU(2)$ algebra at each lattice site. The physical or gauge invariant states are defined to be annihilated by all the $SU(2)$ Gauss’s law constraints at all lattice sites. In literature, these gauge-invariant degrees of freedom are described by the non-local Wilson loops, strings, and hadrons (mesons and baryons). This work adopts the loop-string-hadron (LSH) framework for $SU(2)$ lattice gauge theory [21] as an efficient approach that addresses the challenges associated with a non-abelian gauge theory and non-local interactions.

The LSH framework is a reformulation of Kogut-Susskind’s original framework [27], obtained via the prepotential formalism [30, 31, 32, 33]. The LSH basis states can be intuitively understood to be on-site snapshots of all possible non-local loops of electric fluxes, strings connecting a quark matter, and hadrons (baryons and mesons) that can be present globally on the lattice and satisfy an Abelian Gauss Law (AGL) constraint on each link, ensuring the continuity of electric flux lines. The LSH Hamiltonian consists of the diagonal number operators and ladder operators for the local LSH degrees of freedom and satisfies all the AGLs.

The $SU(2)$ LSH Hamiltonian in $1+1$ dimension has been extensively analyzed in the context of developing efficient quantum algorithms for simulating this theory and it has shown to offer significant reduction in qubit costs and gate depth, for both near and far-term quantum hardware [34].

In contrast, this work presents quantum simulation of LSH dynamics implemented on state-of-the-art 156-qubit IBM quantum processor. The aim of the work is to probe the continuum limit, which requires probing the dynamics in the weak-coupling regime $x \gg 1$ for a lattice of reasonably large size. In this parameter regime, (i) the dynamics is dominated by the off-diagonal term in (2). For an approximation performed for H_E , it affects the dynamics less significantly, as compared to the other coupling regime $x < 1$. (ii) Without any loss of generality, one may consider a lattice with open boundary conditions, where a large number of incoming fluxes just pass through the lattice keeping the global charge sector same as the strong coupling vacuum¹. The contribution of this background fluxes can be approximated as a global phase in this regime. This weak coupling approximate version of the LSH Hamiltonian has previously been developed in the context of analog simulation [35]. The algorithm identifies certain fermionic configurations at a site ($n_i = 0, n_o = 1$), when

¹The symmetry of LSH Hamiltonian preserves the following global charges

(i) total Baryon number: $\mathcal{B} = \sum_{r=0}^{N-1} (n_i(r) + n_o(r)) - N$, and (ii) net lattice flux: $q = \sum_{r=0}^{N-1} (n_o(r) - n_i(r))$. This translate to conserving the global observables $q_o = \sum_{r=0}^{N-1} n_o(r)$ and $q_i = \sum_{r=0}^{N-1} n_i(r)$.

a new flux is created on a link emerging from the lattice, and its electric energy contribution is counted to contribute.

sites following the AGL is given by the on-link constraint

$$\text{Abelian Gauss Law : } n_l + n_o(1 - n_i) \Big|_r = n_l + n_i(1 - n_o) \Big|_{r+1} \quad (3)$$

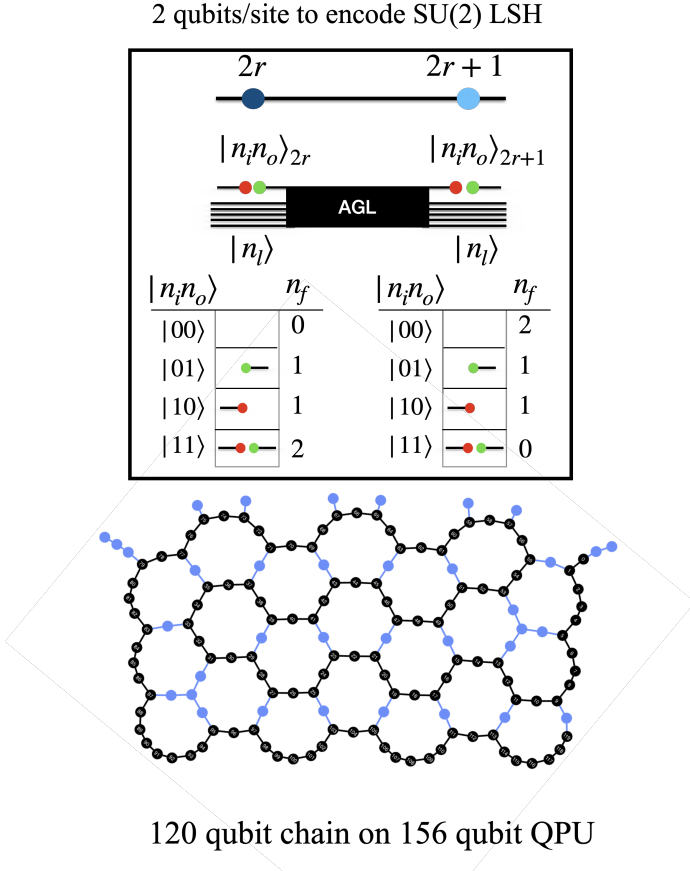


Fig. 1: Encoding physical degrees of freedom to qubits. The local fermion number is defined on the staggered lattice as $n_f(r) = n_i(r) + n_o(r)$ for even sites and $n_f(r) = 2 - [n_i(r) + n_o(r)]$ for odd sites. At any site, $n_f = 2$ denotes the presence of a Baryon, $n_f = 1$ denotes the presence of the end of a meson or a longer string, and $n_f = 0$ denotes the vacuum for fermions. In the left panel, the qubit layout is given. Using the Qiskit Transpiler, the least noisy 120 qubit chain is obtained, which is denoted in black on the hardware layout. This allows one to perform a simulation for a 60-site lattice.

Encoding and preparing the initial states

In a $1 + 1$ -dimensional lattice, electric flux loops can flow in only one direction, and at each site a fermionic doublet can exist. This translates to an on-site physical state at r to be characterized as $|n_l(r), n_i(r), n_o(r)\rangle$. As illustrated in Fig. 1, the manifestly gauge singlet quantum numbers, n_l , denotes the electric flux passing through the site without any change and can vary from zero to infinity; $n_i = 1$, denotes an incoming flux being absorbed at that site by an on-site fermion forming a string-end like object for an incoming string; $n_o = 1$, denotes an outgoing flux being created at that site by an on-site fermion forming a string-end like object for an outgoing string. Fermionic statistics restricts n_i, n_o to take values between $(0, 1)$, while being bosonic, n_l can be any positive semi-definite integer. Abelian weaving across the neighbouring

As a consequence of the fact that gauge field are not dynamical for one spatial dimension, the quantum number n_l across the lattice is determined by the boundary flux and the fermion configurations throughout the lattice in order to satisfy the AGL at all the links of the lattice. This basis, being a strong coupling basis, yields the electric and mass part of the Hamiltonian H_E, H_M to be diagonal terms. While the off-diagonal terms of the Hamiltonian, the matter-gauge interaction H_I , cause the dynamics of loops, strings and hadrons on the lattice.

The initial state is chosen to be an unentangled state, which is a strong coupling eigenstate in LSH basis. A natural choice of such a state is the strong coupling vacuum, which corresponds to a ‘no particle - no antiparticle’ state with $n_f = 0$ at all sites as illustrated for a small lattice in Fig. 2. Next, a different initial state is prepared, where a meson is placed at the middle of the lattice, where $(n_f(r) = 1, r = N/2 - 1, N/2)$, while keeping $n_f = 0$, elsewhere.

Observing Real-time Dynamics

In this work, quench dynamics of a single hadron propagating through a dynamical medium is studied for a spatial lattice with 60-staggered site and for 25-trotter steps. Towards this goal, first, the SCV is prepared and evolved for t_n Trotter steps. Next, the hadronic state is also evolved for the same number of Trotter steps. For both run, the state of the qubits are measured in σ_z basis and the probability of finding it up or down is calculated for a large number of copy of the same experiment. This is repeated for $t_n = 1, 2, 3, \dots, 25$. A schematic representation of the time evolution of such a quantum state is presented in Fig. 2. The probability distribution obtained in the first experiment (the vacuum (SCV) fluctuation) is subtracted from the probability distribution of the time evolution of the hadron placed on the SCV. The experiment’s findings and their benchmarking are presented in the next section and in Fig. 3.

The experimental quantum simulation as well as classically simulated results reveal an early-time breathing mode of hadron, characterized by internal oscillations of cluster formation and decay [25] driven by the highly entangled environment. Extracting the same information from the tensor network calculation is straightforward and reveals an interesting observation towards hadronization of the universe as envisaged in [36, 37]. Continuing the evolution for longer would allow the hadron to reach its critical length for string breaking. String breaking would reduce entanglement. With further time evolution, the entire spatial lattice is expected to get hadronized, a state, with no/minimal long-range entanglement [26].

The experiment on QPU is performed with a circuit of more than 17000+ two-qubit gates and 60000+ single qubit gates, and a fixed 10,000 shot budget per trotter steps. The depth of 2-qubit gates for simulating the Time evolution, grow up to 259 for 20, and to 324 for 25 Trotter steps respectively. Using only a low-cost readout error mitigation [22], the signal from QPU shows a coherent signal for propagation of a hadron by extending its size at each Trotter step, but confined within a ‘light-cone’. The edges of the ‘light cone’ trace a curved path instead of a straight line, denoting the constituent quarks to stay confined by the strong force instead of flying away freely.

The experimental observation is benchmarked by two classical computing methods: (i) Tensor Network (TN) calculations per-

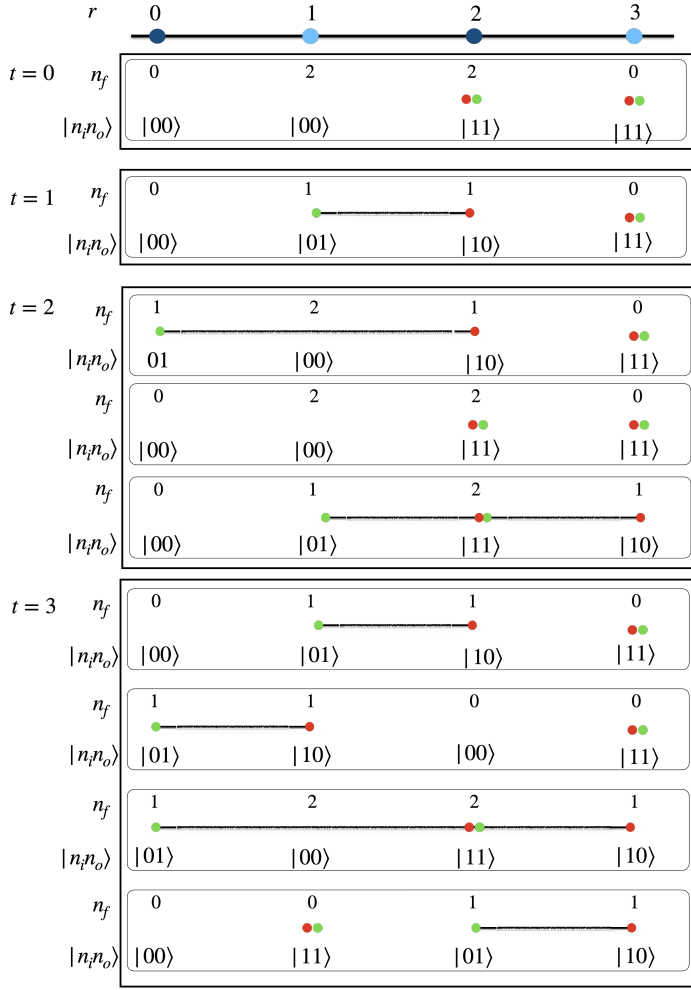


Fig. 2: Schematic of quantum evolution on a 4-site lattice. The diagram illustrates the buildup of entanglement and particle number fluctuations over 3 Trotter steps under the LSH Hamiltonian. The system is initialized at $t = 0$ in a zero-entanglement product state containing two baryons (total fermion number $N_f = 4$). At $t = 1$, the evolution transitions the system to a single meson state ($N_f = 2$). Subsequent steps ($t = 2, 3$) generate increasingly complex superpositions of states with varying particle numbers ($N_f \in \{2, 4, 6\}$), governed by the interplay of the electric (H_E) and mass (H_M) Hamiltonian terms. This fluctuation of total particle number is a hallmark of relativistic quantum field theory. Each basis state is represented as $\otimes_r |n_i, n_o\rangle_r$ and mapped directly to qubit registers. The values of n_f across the lattice at all time steps are measured to construct the experimental heatmaps presented in this work. The branching of the wavefunction depicted here highlights the rapid growth of entanglement, rendering the full 120-qubit simulation classically intractable.

formed for the original LSH Hamiltonian and basis, via construction of Matrix Product Operators (MPO) and Matrix Product States (MPS) respectively, carefully created as a toolbox for LSH calculations [38]. The time evolution is computed using a 2-site TDVP algorithm that is free of Trotterization error. The bosonic cut-off for this computation is set at $2j_{max} = 6$, while a cut-off in bond dimension is set at $D_{max} = 200$. This method, albeit ap-

proximate, has been checked to provide acceptable convergence up to the time limit observed. (ii) A recently developed algorithm to classically simulate a quantum circuit, the Pauli Propagation Method (PPM) [23], is employed to simulate noiseless simulation of the circuit for 120 qubits. This method involves careful operator backpropagation via identifying the gate operations and qubits responsible for each measurement. The approximation of this method is due to the use of a finite number of Pauli terms in the operator expansion. The maximum of this number is calculated by extrapolating the exact number of Pauli terms for the circuit with lower gate depths (first few Trotter steps) to minimise error due to truncation of terms.

Fig. 3 shows a comparison for the observables obtained from the experimental observations from quantum simulation on IBM Boston, tensor network calculation performed for the full LSH Hamiltonian and classical simulation of the quantum circuit via the Pauli propagation method. While the heatmap for the first two agrees strikingly, further investigation yields a complete match between the two classical methods, suggesting that the approximations performed on the original theory to make an implementable circuit are valid. Comparison between the noiseless simulation of quantum circuit via PPM and the experimental results demonstrates the effect of noise (the background beyond the lightcone has some non-zero values), but also establishes that the observables remain largely noise resilient even for the QPU in the pre-fault tolerant era. Fig. 3 thus not only validates the experimental observation's resilience to noise, but also the validity of the weak coupling approximation and the associated quantum algorithm. Comparison of the time taken for each Trotter step using classical and quantum algorithms shows a clear separation of scale, and the same leads to even wider separation for a complete simulation of dynamics up to a fixed time.

It is worth comparing the time required to obtain the data expressed in Fig. 3 using classical and quantum algorithms and devices: (i) classical algorithm implemented on a classical computer, (ii) quantum algorithm, simulated on a classical computer and (iii) quantum algorithm implemented on a quantum hardware for a fixed number of shots. (i) The tensor network experiment on classical computing hardware is subjected to an entanglement wall. The time complexity grows exponentially with the entanglement entropy. Ideally, it requires growing value for the allowed maximum bond dimension D_{max} in order to minimise the error. In this work, D_{max} was allowed to grow up to 200, due to constraints with available computing resources. With this particular limit on D_{max} , the dynamics beyond 20 Trotter steps are obtained to contain errors which can not be neglected. Visually, the heat map of simulated dynamics shows error when compared to the same obtained from the QPU. The details are reported as supplementary information. In summary, TN calculations are not useful for computing dynamics for longer times as the coupling $x \rightarrow \infty$ with finite computing resources. (ii) The quantum simulation continues to perform effortlessly in the high entanglement domain and demonstrates coherence. Invading long-time dynamics for $x \rightarrow \infty$ is not a challenge for quantum computer except for the loss of coherence due to noise. The reported dynamics of the observable depicts noise resilience, due to the differential measurement protocol employed in this experiment. The compute time on QPU, which is 20 seconds for each time step and depends primarily on the number of shots. For our experiments, we have used a fixed budget of 10,000 shots. The Pauli propagation method [23] provides an efficient classical algorithm to simulate the error-free quantum circuit classically. This method is used with an estimate of max-term obtained via extrapolations of exact results for small size systems to mini-

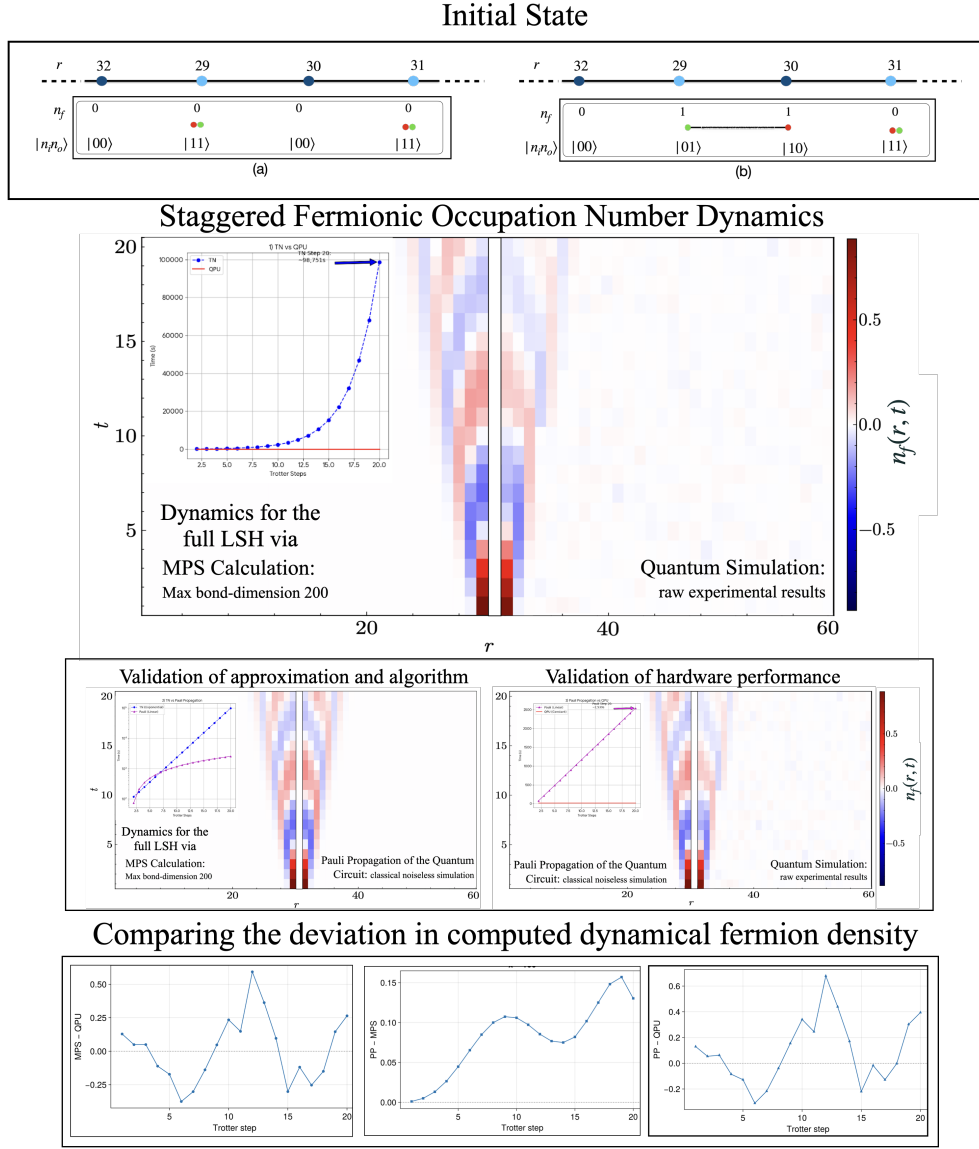


Fig. 3: Real Time Propagation of SU(2) Hadron: validation of the ansatz, algorithm, and implementation on hardware. The top panel displays a cartoon representation of the initial states; (a) The strong coupling vacuum for a staggered lattice, and (b) A meson is placed at the middle of the lattice on top of the strong coupling vacuum. The fermion/antifermion number $n_f = 0$ at all sites except at two middle sites of (b), which are both singly occupied and are characterized by $n_f = 1$. The lower panels shows the light-cone propagation of a meson (t vs. lattice site r) placed at the center of the lattice at $t = 0$. The fermion density n_f for the time evolution of the state (a) subtracted from (b) in the same, is plotted for 20 time steps. Space-time evolution of particle density n_f on a 60-site lattice is compared using three different approaches: (i) Quantum simulation on IBM Boston using only measurement error mitigation, (ii) Tensor network calculation using the MPS and MPO constructed for the full LSH Hamiltonian and using 2-site TDVP algorithm. (ii) Pauli Propagation method applied for the classical simulation of the quantum circuit. The dynamics on the left half of the figure (lattice sites 0 – 29) are from one calculation, while the right half of the plot shows another. The visible agreement confirms the validity of the experimental result as simulation of the full LSH. Moreover, the MPS calculation is performed for the full LSH Hamiltonian and uses the TDVP algorithm to avoid Trotterization error. The Quantum simulation is performed using the weak-coupling approximated LSH and first-order Trotterization. The visible match between the left and right sides of the plot validates both approximations in the scaled-up experiment. In the inset of each plot, the clock time taken for each method is compared (for MPS, projected time with exponential scaling is shown). Our QPU time for a fixed budget of $10k$ shots per trotter step, was a constant 20 seconds per trotter step; the same for the Pauli Propagation method increased linearly on a CPU and for the tensor network method increased exponentially (the last few steps were constant as the bond dimension was kept constant). The relative deviation in average fermion density is compared in the bottom panel.

mize truncation error. The simulation time of PPM *on a CPU* grows linearly with the number of trotter steps. In general, the Pauli propagation method works efficiently for a circuit with high entanglement but low magic. While the quantum algorithm involved in this particular simulation not only causes a growth of entanglement entropy via its two-qubit gate operations (as extracted from the tensor network calculations), it also contains a significant amount of non-Clifford gate operations.

The quantum simulation protocol is further tested for a couple of different values of coupling $x \rightarrow x/2$ and $x \rightarrow 2x$, without changing the value of m/g . The experimental observation confirms the expected ‘shrinking’ and ‘widening’ of light cone structure in Hadron propagation respectively as shown in Supplemental material, confirming the robustness of the algorithm, implementable on QPU. Simulation of the full LSH dynamics is attempted using tensor network for $x = 50, 200$, while the noiseless simulation of the quantum circuit for both cases is performed with Pauli propagation. The results are summarized in Fig. 4. Despite being classically simulatable for the same circuit with the same gate depth, the classical simulation experienced increased time complexity (an increased slope under linear scaling) on a CPU as x increased, suggesting the growth of non-Clifford operations as the continuum limit of the theory is approached. Tensor network calculation, on the otherhand worked almost flawlessly for $x = 50$, struggled a for $x = 100$, and almost completely broke down for $x = 200$ as evident in the entanglement dynamics captured by the TN calculation and presented in Fig. 4. The PPM, executed with finite number of allowed Pauli terms in the algorithm deviates from the exact analysis, and the same is reflected in violation of globally conserved charges by PPM, that is again absent for $x = 50$, starts to emerge from $x = 100$, and becomes even more prominent for $x = 200$.

Classical algorithms, when based on tensor network, faces the entanglement wall, while a classical simulation of quantum circuit is limited by the magic present in the circuit. Whereas quantum processors have limitations arising for noise and not the same limitations from entanglement or magic, and thereby provide an alternative pathway to perform these computations.

Outlook

The current work paves the way for performing ab initio calculations in quantum chromodynamics using a quantum computer, and demonstrates that scalable quantum simulations of non-Abelian gauge theories are feasible even in the pre-fault-tolerant era, beyond proof-of-concept experiments.

By successfully accessing a 60-site lattice, the current work establishes that pre-fault-tolerant hardware, when combined with hardware-efficient encodings such as LSH and error-robust measurement protocols, can capture non-perturbative dynamics inaccessible to classical methods. This success opens several distinct avenues for future research.

First, extending the simulation time beyond the current window is an immediate priority. Our results hint at the early stages of hadron breathing and entanglement growth; prolonging the evolution would allow for the direct observation of string breaking and the subsequent hadronization of the vacuum—phenomena that are central to understanding the thermalization of the quark-gluon plasma formed in heavy-ion collisions [25, 36, 26].

Second, the LSH framework utilized here is naturally extensible to higher dimensions and more complex gauge groups. The most significant barrier to simulating Quantum Chromodynamics (QCD) has been implementing the SU(3) gauge group. The methods validated in this work for SU(2) provide a blueprint for

advantage in encoding SU(3) gauge theory to qubits via LSH framework built upon the prepotential formulation [39]. The 1+1-dimensional framework is ready to use [40], while the higher-dimensional framework is being developed step by step [41, 42].

Finally, the efficient encoding and the error-resilient differential observation technique used in this work, and confirmation of its validity in capturing correct physical dynamic establishes a pathway for computing novel real-time dynamics [43]. As hardware fidelities continue to improve, and with thoughtful incorporation of active error mitigation or early error-correction protocols, these methods are expected to enable increasingly sophisticated simulations of scattering phenomena. When applied to finite-density systems where the Monte Carlo sign problem is most severe, could soon unravel the phase diagram of dense nuclear matter, shedding light on the interiors of neutron stars and the early universe. The observation of the dynamical evolution of the entanglement entropy in Fig. 4, obtained via tensor network calculation, reveals the signature of the pre-Hadronisation phase (hadron passing through a highly entangled region) of the universe probed within the time scale reported. Allowing the dynamics for longer and with a larger number of probes may lead to simulating hadronisation in the early universe. Furthermore, enhancement of this work can lead to the ability to study collisions of mesons and baryons and to probe parton distribution functions and deep-inelastic scattering processes from first principles would mark a substantial expansion in the range of non-equilibrium quantum field theory calculations accessible to computation, extending beyond what is currently practical with classical lattice QCD techniques.

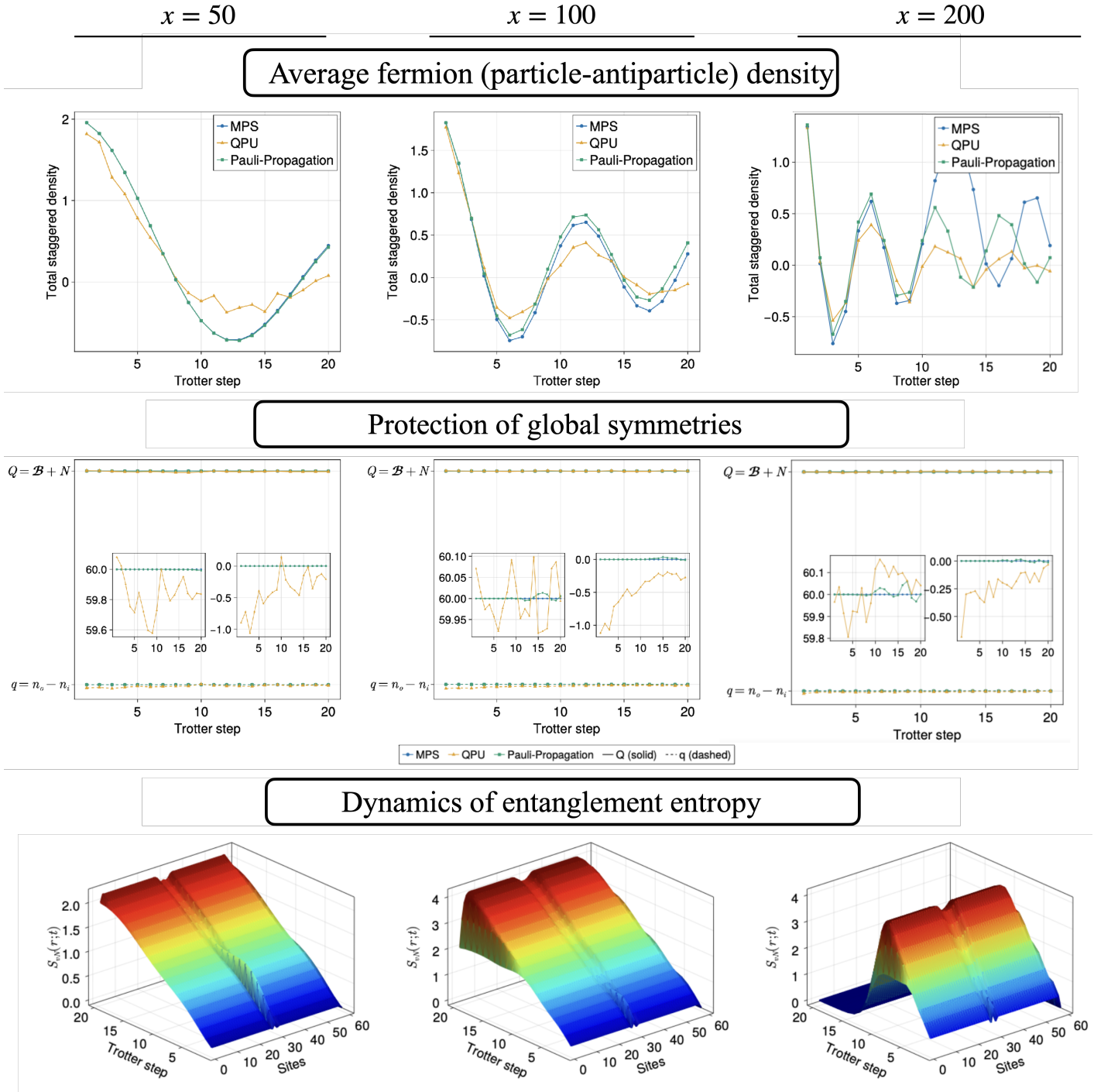


Fig. 4: Comparing robustness of quantum simulation versus classical simulation towards $x \rightarrow \infty$. Top row: The dynamics of average fermion density is plotted with time. For $x = 50$, MPS and PPM agree exactly, QPU shows deviation but follow the trend. For $x = 100$, MPS and PPM start to separate out after 5th Trotter steps, QPU deviates but follows the trend. For $x = 200$, post 10th Trotter step, MPS and PPM do not follow the same trend, QPU follows PPM, with deviation. Middle row: The conservation of global charges are tracked for all simulation. Overall it stays conserved in all the methods. As presented in the insets, QPU shows a small deviation, for all x values. MPS preserves the global constraints by construction [38]. PPM shows small deviation, and it increases with increasing x . Bottom row: The entanglement entropy, obtained via TN calculation, shows linear growth for $x = 50$, saturates to a plateau for $x = 100$, while the allowed bond dimension fails to handle entanglement growth for $x = 200$ case, and in effect the MPS simulation fails to capture physics anymore. The drop in entanglement is an artifact of finite bond dimension, rather than being a physical phenomenon.

Methods

The theory to be simulated

In this section, we briefly review the theory we aim to simulate, the Kogut-Susskind Hamiltonian formalism, represented in the loop-string-hadron basis. As discussed in the main text, the continuum limit weak-coupling regime of the theory, encoded in the gates of the current experiment.

Kogut-Susskind Hamiltonian

The scaled Kogut-Susskind (KS) Hamiltonian describing SU(2) Yang Mills theory coupled to staggered fermions on (1+1)-d (1d spatial lattice and continuous time) [27] can be written as:

$$W = H_E^{(KS)} + \mu H_M + x H_I^{(KS)}. \quad (4)$$

The gauge link $U(r)$ is a 2×2 unitary matrix defined on the link connecting sites r and $r+1$. A temporal gauge is chosen to derive the above Hamiltonian, which sets the gauge link along the temporal direction equal to unity. The color electric fields $E_{L/R}^a$ are defined at the left L and right R sides of each link, and they satisfy the following commutation relations (SU(2) algebra) at each end:

$$\begin{aligned} [E_L^a(r), E_L^b(r')] &= i\epsilon^{abc}\delta_{jr'}E_L^c(r), \\ [E_R^a(r), E_R^b(r')] &= i\epsilon^{abc}\delta_{rr'}E_R^c(r'), \\ [E_L^a(r), E_R^b(r')] &= 0, \end{aligned} \quad (5)$$

where ϵ^{abc} is the Levi-Civita symbol. The electric fields and the gauge link satisfy the following quantization conditions at each site,

$$\begin{aligned} [E_L^a(r), U(r')] &= -\frac{\sigma^a}{2}\delta_{rr'}U(r), \\ [E_R^a(r), U(r')] &= U(r)\delta_{rr'}\frac{\sigma^a}{2}, \end{aligned} \quad (6)$$

where σ^a are the Pauli matrices. The Hamiltonian in (4) is gauge invariant as it commutes with the Gauss' law operator,

$$G^a(r) = E_L^a(r) + E_R^a(r-1) + \psi^\dagger(r)\frac{\sigma^a}{2}\psi(r) \quad (7)$$

at each site r . The physical sector of the Hilbert space corresponds to the space consisting of states annihilated by (7). Solving the non-Abelian Gauss laws at each site r as given in (7) is non-trivial, and engineering the same in an experiment is the most difficult job.

LSH Hamiltonian

LSH formalism of lattice gauge theory is based on prepotential framework, where, the original canonical conjugate variables of the theory, i.e color electric field and link operators are replaced by a set of harmonic oscillator doublets, defined at each end of a link [44, 45, 46, 47, 48, 49, 39, 50, 51]. In prepotential framework, the SU(2) gauge group is confined to each lattice site allowing one to have local gauge invariant operators and states at each site, leading to a description of local loop segments. Combining prepotentials with staggered fermionic matter fields at each lattice site to form gauge invariant singlets, yields on-site string-end operators. Staggered matter fields also combine into local gauge-invariant configurations representing hadrons,

likewise in the original understanding of the theory. Thus the gauge invariant and orthonormal LSH basis is characterized by a set of three integers $n_l(r), n_i(r), n_o(r)$, corresponding to the loop, incoming string, and outgoing string at each site (on-site hadron is equivalent to simultaneous presence of both the string ends). LSH basis states satisfy all the Gauss' law constraints by the construction. The allowed values of the LSH quantum numbers are

$$0 \leq n_l(r) \leq \infty, \quad 0 \leq n_i(r) \leq 1, \quad 0 \leq n_o(r) \leq 1, \quad (8)$$

denoting n_l to be a bosonic excitation, whereas n_i, n_o to be fermionic in nature, even though the string ends contain information of both gauge field and matter content.

A set of LSH operators consisting of both diagonal and ladder operators are defined locally at each site as:

$$\hat{n}_{l/i/o}|n_l, n_i, n_o\rangle = n_{l/i/o}|n_l, n_i, n_o\rangle \quad (9)$$

$$\hat{\lambda}^\pm|n_l, n_i, n_o\rangle = |n_l \pm 1, n_i, n_o\rangle \quad (10)$$

$$\hat{\chi}_{i/o}^+|n_l, n_i, n_o\rangle = (1 - \delta_{n_{i/o}, 1})|n_l, n_{i/o} + 1, n_{o/i}\rangle \quad (11)$$

$$\hat{\chi}_{i/o}^-|n_l, n_i, n_o\rangle = (1 - \delta_{n_{i/o}, 0})|n_l, n_{i/o} - 1, n_{o/i}\rangle \quad (12)$$

The LSH basis states must satisfy the AGL, as explained in the main text to be counted as a valid loop-string-hadron segment of the global loop configurations present on the lattice.

Hamiltonian of the theory,

$$W^{(LSH)} = H_E^{(LSH)} + \mu H_M^{(LSH)} + x H_I^{(LSH)} \quad (13)$$

is exactly equivalent to the original Hamiltonian (4), with the following form of electric term, mass term and matter-gauge interaction term in terms of LSH operators:

$$\begin{aligned} H_E^{(LSH)} &= \sum_{r=0}^{N-2} \left[\frac{\hat{n}_l(r) + \hat{n}_o(r)(1 - \hat{n}_i(r))}{2}, \right. \\ &\quad \left. \times \left(\frac{\hat{n}_l(r) + \hat{n}_o(r)(1 - \hat{n}_i(r))}{2} + 1 \right) \right] \end{aligned} \quad (14)$$

$$H_M^{(LSH)} = \sum_{r=0}^{N-1} (-1)^r (\hat{n}_i(r) + \hat{n}_o(r)), \quad (15)$$

$$\begin{aligned} H_I^{(LSH)} &= \sum_{r=0}^{N-1} \frac{1}{\sqrt{\hat{n}_l(r) + \hat{n}_o(r)(1 - \hat{n}_i(r)) + 1}} \times \\ &\quad \left[S_o^{++}(r) S_i^{+-}(r+1) + S_o^{--}(r) S_i^{+}(r+1) \right. \\ &\quad \left. + S_o^{+-}(r) S_i^{--}(r+1) + S_o^{-+}(r) S_i^{++}(r+1) \right] \\ &\quad \times \frac{1}{\sqrt{\hat{n}_l(r+1) + \hat{n}_i(r+1)(1 - \hat{n}_o(r+1)) + 1}}. \end{aligned} \quad (16)$$

Here (16) contains LSH ladder operators in the following combinations (suppressing the explicit site index),

$$S_o^{++} = \hat{\chi}_o^+(\lambda^+)^{\hat{n}_i} \sqrt{\hat{n}_l + 2 - \hat{n}_i} \quad (17)$$

$$S_o^{--} = \hat{\chi}_o^-(\lambda^-)^{\hat{n}_i} \sqrt{\hat{n}_l + 2(1 - \hat{n}_i)} \quad (18)$$

$$S_o^{+-} = \hat{\chi}_i^+(\lambda^-)^{1-\hat{n}_o} \sqrt{\hat{n}_l + 2\hat{n}_o} \quad (19)$$

$$S_o^{-+} = \hat{\chi}_i^-(\lambda^+)^{1-\hat{n}_o} \sqrt{\hat{n}_l + 1 + \hat{n}_o} \quad (20)$$

and

$$S_i^{+-} = \hat{\chi}_o^-(\lambda^+)^{1-\hat{n}_i} \sqrt{\hat{n}_l + 1 + \hat{n}_i} \quad (21)$$

$$S_i^{-+} = \hat{\chi}_o^+(\lambda^-)^{1-\hat{n}_i} \sqrt{\hat{n}_l + 2\hat{n}_i} \quad (22)$$

$$S_i^{--} = \hat{\chi}_i^-(\lambda^-)^{\hat{n}_o} \sqrt{\hat{n}_l + 2(1 - \hat{n}_o)} \quad (23)$$

$$S_i^{++} = \hat{\chi}_i^+(\lambda^+)^{\hat{n}_o} \sqrt{\hat{n}_l + 2 - \hat{n}_o}. \quad (24)$$

The strong coupling ($x \gg 1, m/g = \text{fixed}$) vacuum of the LSH Hamiltonian is given by:

$$\begin{aligned} n_l(r) &= 0 \quad \forall r \\ n_i(r) &= 1, \quad n_o(r) = 1 \quad \text{for } r \text{ odd} \\ n_i(r) &= 0, \quad n_o(r) = 0 \quad \text{for } r \text{ even} \end{aligned} \quad (25)$$

which satisfy AGL on all the links. The spectrum and dynamics of the LSH Hamiltonian is obtained identical to the gauge invariant dynamics of the Kogut susskind Hamiltonian with the same value of bosonic cut-off using exact diagonalization [52]. The tensor network calculations reported in this work are based on the LSH framework and uses a bosonic cut-off $j_{max} = 5/2$, using the tensor network toolbox [38].

Approximations for weak coupling regime

We focus on open boundary condition, and allow an incoming flux l_i to enter the lattice. Using AGL on each link, the value of n_l at each site can be fully determined as

$$\begin{aligned} n_l(r) &= l_i - n_i(r)(1 - n_o(r)) + \sum_{r'=0}^{r-1} (n_o(r') - n_i(r')) \\ &\approx l_i - n_i(r)(1 - n_o(r)) \quad \text{for } l_i \gg 0. \end{aligned}$$

Thus any physical state in LSH formalism in one spatial dimension is completely determined by (n_i, n_o) quantum numbers at each site and the interaction can be approximated to be local. This approximation is valid [35] if we focus on the weak coupling regime $x \gg 1$, and the off-diagonals contribute more to the dynamics. Choosing the global charge sector same as that of the SCV i.e. with no net Baryon number and no net lattice flux $(\mathcal{B}, q) = (0, 0)$, the minimum energy strong coupling configuration of the string-ends still remain the same as the SCV.

We further make an approximation of

$$\frac{n_l}{n_l + 1} \rightarrow 1 \quad \& \quad \frac{n_l + 1}{n_l + 2} \rightarrow 1$$

for all the prefactors appearing in H_I^{LSH} considering the $l_i \gg 1$ scenario.

Within this approximation, the total electric part of the LSH Hamiltonian is given by:

$$H_E^{\text{(approx)}} = \frac{g^2 a}{2} \left[N h_E^0 + \sum_{\{r'\}} \left(\frac{l_i}{2} + \frac{3}{4} \right) \right] \quad (26)$$

where, $\{r'\}$ denotes the sites with fermionic configuration $n_i(r') = 0, n_o(r') = 1$ and h_E^0 , corresponds to a global phase due to the background flux.

Mass Hamiltonian: The mass term (15), being independent of gauge field configuration remain the same in the weak coupling approximation.

$$H_M^{\text{(approx)}} = \sum_r (-1)^j (\hat{n}_i(r) + \hat{n}_o(r)) \quad (27)$$

Interaction Hamiltonian: The matter-gauge field interaction term is the most complicated within LSH framework as detailed in (16). In the strong coupling limit of the theory, this particular term gives small contribution to the Hamiltonian. However, in the weak coupling regime of interest, this term becomes significant. The approximation scheme that we follow casts the interaction Hamiltonian given in (16) as,

$$\begin{aligned} H_I^{\text{(approx)}} &= \sum_r \left[\chi_o^+(r) \chi_o^-(r+1) + \chi_o^+(r+1) \chi_o^-(r) \right. \\ &\quad \left. + \chi_i^+(r) \chi_i^-(r+1) + \chi_i^+(r+1) \chi_i^-(r) \right] \end{aligned} \quad (28)$$

The purpose of the present approximation scheme is to bring the interaction Hamiltonian into simple form, yet describing matter gauge dynamics in the weak coupling regime reliably.

In the next section, we present the quantum algorithm construction, starting with the mapping of LSH quantum numbers to the hardware's qubits and mapping the time evolution unitary for the weak coupling approximated Hamiltonian to a quantum circuit.

Algorithm for QPU

In this work we study the time evolution of the system for a scaled time τ for the scaled Hamiltonian W cause by the unitary operator

$$U(t) = \exp -iHt = \exp -iW\tau \quad (29)$$

$$\text{where,} \quad W = 2xa^3 H \Rightarrow \tau = \frac{t}{2xa^3} \quad (30)$$

For Trotterized time evolution, the total time $\tau = N_\tau \delta\tau$, where N_τ denotes the number of Trotter steps. If the value of the coupling changes, i.e. $x \rightarrow x'$, the scaled time

$$\tau \rightarrow \tau' = \frac{x}{x'} \tau \Rightarrow N'_\tau \delta\tau' = \frac{x}{x'} N_\tau \delta\tau. \quad (31)$$

If a Trotterized time evolution is performed without changing the size of the Trotter steps (i.e. $\delta\tau' = \delta\tau$), the number of Trotter steps required for evolving the system for a fixed duration of physical time is given by

$$N'_\tau = \frac{x}{x'} N_\tau. \quad (32)$$

We employ a first-order-Trotterized Schrödinger time evolution operator for unitaries constructed for

$$xH_I^{\text{approx}}, \quad H_E^{\text{approx}} \quad \& \quad \mu H_M^{\text{approx}}$$

in that order, over a very short time δ_τ for each Trotter step. Evolving the system through N_τ steps span a total time of $\tau = N_\tau \delta_\tau$. We choose δ_τ to be very short to minimize the Trotterization error and keep the same fixed to 0.0015 through the work.

Mapping string-ends to qubits

An open-boundary lattice of N sites is simulated on $2N$ qubits. The numbers $n_i(r)$ and $n_o(r)$ are directly mapped to individual qubits, whereas the $n_l(r)$ numbers can be recovered using (26). To make the qubits effectively fermions, the Jordan-Wigner transformation maps the ladder operators:

$$\begin{aligned} \hat{\chi}_i^-(r) &= \sigma^+(r) \prod_{r' < r} (-\sigma^z(r')) \\ \hat{\chi}_o^-(r) &= \sigma^+(r+L) \prod_{r' < r+N} (-\sigma^z(r')), \end{aligned} \quad (33)$$

where the qubit ladder operators are defined as

$$\begin{aligned} \sigma^+ &= \begin{pmatrix} 0 & 1 \\ 0 & 0 \end{pmatrix} \Rightarrow \sigma^+ |0\rangle = \sigma^+ \begin{pmatrix} 1 \\ 0 \end{pmatrix} = 0, \\ \sigma^+ |1\rangle &= \sigma^+ \begin{pmatrix} 0 \\ 1 \end{pmatrix} = \begin{pmatrix} 1 \\ 0 \end{pmatrix}. \end{aligned} \quad (34)$$

The Hermitian conjugates are $\hat{\chi}_i^+(r) = (\hat{\chi}_i^-(r))^\dagger$ and $\hat{\chi}_o^+(r) = (\hat{\chi}_o^-(r))^\dagger$, with $\sigma^- = (\sigma^+)^\dagger$.

The implied ordering of the variables where the first N represent the n_i quantum numbers, and the last N the n_o numbers, is relevant only within the mathematical construction, providing, for example, $\hat{\chi}^+ \hat{\chi}^-$ products and the indices in matrix calculations. When considering the actual mapping to the hardware's qubits, a different ordering can be used. The qubit layout we choose is a zigzag sequence of i and o quantum numbers:

$$|q_{2r}\rangle \equiv |n_i(r)\rangle, \quad |q_{2r+1}\rangle \equiv |n_o(r)\rangle. \quad (35)$$

This minimizes the number of SWAP layers throughout the circuit. Each $n_i(r)$ number needs to interact with both of its i neighbours, $n_i(r-1)$ and $n_i(r+1)$, and similarly for o numbers, while the electric Hamiltonian term acts on the $i-o$ pairs. All the SWAP gates required to enable this interaction can be arranged in two layers only for each trotter step (see Fig. 6), making this a highly efficient encoding whose depth depends only on the number of trotter steps, and not on the lattice site. Note that, in the initial Trotter step, the first layer of gates would have been the SWAPs to get the first interaction pairs adjacent, so the actual qubit initialization has an ordering that absorbs these SWAPs: $n_i(0), n_i(1), n_o(0), n_o(1), n_i(2), n_i(3), n_o(2), n_o(3), \dots$, while the layout at the end of each Trotter step follows the zigzag ordering above.

Building the Quantum Circuit for Time evolution

A single Trotter step applies the unitary

$$U(\delta_\tau, c, \tilde{m}, \theta) \underset{\text{small } \delta_\tau}{\approx} e^{-i\delta_\tau H'} e^{-i\tilde{m}H_M} e^{-i\delta_\tau H_E} e^{-icH_I} \quad (36)$$

where $c = \delta_\tau x$, $\tilde{m} = \delta_\tau \mu$ are parameters appearing in the corresponding unitaries due to the interaction, and mass parts of the Hamiltonian.

The interaction part given in (28) translates into its qubit version as

$$H_I^{\text{approx}} = - \sum_{\substack{r=0 \\ r \neq N-1}}^{2N-2} [\sigma^-(r)\sigma^+(r+1) + \sigma^+(r)\sigma^-(r+1)] \quad (37)$$

The corresponding unitary takes the form

$$\begin{aligned} U_I &= e^{-i\delta_\tau x H_I} \\ &\underset{\text{small } \delta_\tau}{\approx} \prod_{r \neq N-1} \exp [ic (\sigma^-(r)\sigma^+(r+1) + \sigma^+(r)\sigma^-(r+1))] \\ &= \prod_{r \neq N-1} \exp \left[ic \begin{pmatrix} 0 & 0 & 0 & 0 \\ 0 & 0 & 1 & 0 \\ 0 & 1 & 0 & 0 \\ 0 & 0 & 0 & 0 \end{pmatrix}_{r \otimes r+1} \right] \\ &= \prod_{r \neq N-1} \begin{pmatrix} 1 & 0 & 0 & 0 \\ 0 & \cos c & i \sin c & 0 \\ 0 & i \sin c & \cos c & 0 \\ 0 & 0 & 0 & 1 \end{pmatrix}_{r \otimes (r+1)} \end{aligned} \quad (38)$$

Here $c = \delta_\tau x$ is a real constant. Since each non-boundary-site qubit appears in two of the factors, corresponding to hopping in two directions, the algorithm is split into two layers with SWAP gates in between. Using matrix multiplication, the two-qubit

hopping term is uncovered in terms of standard single- and two-qubit gates:

$$\begin{aligned} U_{I, r \otimes (r+1)} &= CNOT_{(r+1) \otimes r} (1 \otimes H) CNOT_{r \otimes (r+1)} \\ &\quad (1 \otimes R_z(c)) CNOT_{r \otimes (r+1)} (1 \otimes R_z(-c)) \\ &\quad (1 \otimes H) CNOT_{(r+1) \otimes r} \end{aligned} \quad (39)$$

After the two layers of this hopping unitary, SWAP gates get the qubits into the zigzag position for the electric and mass terms to be applied.

The electric part is

$$H_E = N h_E^0 + \sum_{\{r'\}} \left(\frac{n_l}{2} + \frac{3}{4} \right) \quad (40)$$

with $\{r'\}$ denoting the set of sites in the fermion configuration 01 (corresponding to the second entry in the 2-qubit tensor product). The first term gives a global phase to the evolution of qubits, so we ignore it. This is also an approximation because the value of the average flux h_E^0 differs between basis states, but we approximate it to always be equal to the boundary flux. However, the phase correction in the 01 case at every site and its entangling properties can be seen to increase the validity of the simulation. This second term in H_E is translated into a circuit applied on each site's qubit pair, which gives a certain phase in the required 01 case, and a different phase in the other three cases (same for all three):

$$\begin{aligned} U_{E, x \otimes (x+1)}(\theta) &= (r \otimes R_z(\theta/2)) CNOT_{x \otimes (x+1)} (1 \otimes R_z(-\theta/2)) \\ &\quad CNOT_{x \otimes (x+1)} (R_z(\theta/2) \otimes 1) (r \otimes 1) \\ &= \begin{pmatrix} e^{-i\theta/4} & 0 & 0 & 0 \\ 0 & e^{i3\theta/4} & 0 & 0 \\ 0 & 0 & e^{-i\theta/4} & 0 \\ 0 & 0 & 0 & e^{-i\theta/4} \end{pmatrix}_{x \otimes (x+1)} \end{aligned} \quad (41)$$

which is a global phase plus an $e^{i\theta}$ phase in the desired case. The x and $x+1$ here correspond to the n_i, n_o pair of any single lattice site.

θ can be identified from the desired phase

$$e^{-i\delta_\tau \left(\frac{n_l}{2} + \frac{3}{4} \right)} = e^{i\theta} \implies \theta = -\delta_\tau \left(\frac{n_l}{2} + \frac{3}{4} \right) \quad (42)$$

The mass term H_M adds a phase to each qubit:

$$\mu H_M = \mu \sum_r (-1)^r (n_i(r) + n_o(r)) \quad (43)$$

$$\begin{aligned} e^{-i\delta_\tau \mu H_M} &= \prod_r e^{i(-1)^{r+1} \tilde{m} n_i(r)} e^{i(-1)^{r+1} \tilde{m} n_o(r)} \\ &= \prod_{r \text{ even}} R_z(-\tilde{m})_{2r} R_z(-\tilde{m})_{2r+1} \\ &\quad \prod_{r \text{ odd}} R_z(\tilde{m})_{2r} R_z(\tilde{m})_{2r+1} \end{aligned} \quad (44)$$

where $\tilde{m} = \delta_\tau \mu$. The R_z gates are applied at the end of each Trotter step.

Proof of Concept

The algorithm is simulated classically for small numbers of qubits. For a 6-site lattice (12 qubits), ideal simulation of the quantum circuit is compared to exact diagonalization results by plotting the total particle number over time for both cases. Exact diagonalization takes the full LSH Hamiltonian as given in

(14), (15) and (16). The calculation of dynamics is also exact via simple matrix multiplication, and free from any Trotterization approximation. Comparison of the dynamics for the original theory and the same obtained via ideal simulation of the quantum circuit is presented in Fig. 5.

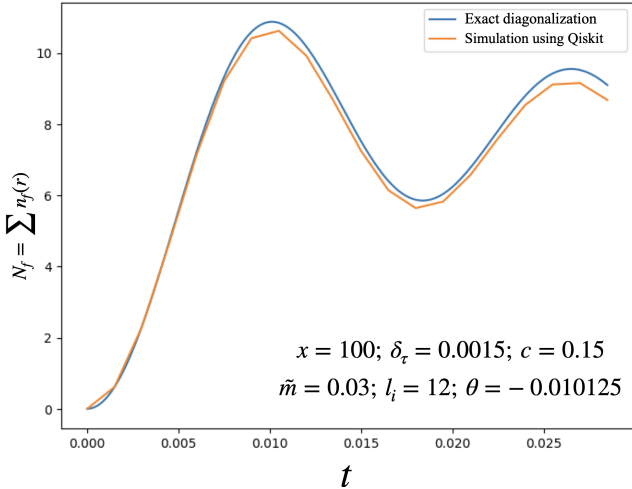


Fig. 5: Proof of concept. Particle number for a lattice of 8 sites as calculated from qubit expectation values at each Trotter step using Qiskit simulator, compared with the exact diagonalization result for the full LSH Hamiltonian, which is free from any Trotterization error and approximation error. Parameters in the quantum circuit are chosen to reproduce the intended regime of the theory with $x = 100$ and $m/g = 1$. The initial state is chosen to be the strong coupling vacuum, which is a computational basis state.

Scaling up the quantum simulation

With the benchmarking of the parameters as presented in Fig. 5, we proceed towards large scale implementations of the quantum circuit (Fig. 6) using IBM BOSTON (156 qubit HERON processor).

Experimental measurement from QPU

We implement trotterized time evolution with a circuit depth that is independent of system size. Each Trotter step comprises two SWAP layers to mediate nearest-neighbor interactions; for steps $t_{\text{rot}} \geq 2$ we prepend a single additional SWAP layer to account for the initial zigzag configuration of qubits. Because the circuit layout is isomorphic to the device topology, qubit mapping requires no extra SWAPs. The Qiskit transpiler is used solely to (i) select a low-noise linear chain of physical qubits and (ii) decompose the circuit to the native gate set of the device.

At each Trotter step, we estimate $\langle \sigma_z \rangle$ for every qubit and infer the excited-state occupancy via $P(1) = \frac{1 - \langle \sigma_z \rangle}{2}$. Expectation-value estimation enables error-mitigation workflows, and keeps the path open for future application of state-of-the-art error mitigation; in this work we apply measurement-error mitigation to correct readout bias. Following these strategies, we simulate a 60-site staggered SU(2) lattice using 120 qubits (two qubits per site). The two-qubit depth for t Trotter steps is $13t - 1$, where the -1 accounts for a bypassed SWAP layer enabled by the zigzag qubit initialization. Thus, at $t = 25$, the circuit has

two-qubit depth 324 and comprises 17,660 two-qubit gates with a total gate count of 90,955.

No exact classical method is available at this scale. For validation, we compare the hardware results against tensor-network simulations and a Pauli-propagation method.

Benchmarking via TN

In this section, we briefly outline the Matrix Product State (MPS) ansatz used to benchmark the QPU results. Classical Tensor Network (TN) methods have emerged as powerful tools to study properties of low-dimensional quantum systems [53, 54]. Of late, they have been used to explore static and dynamic properties of lattice gauge theories, see Ref.[55] for a comprehensive review on this topic. In this context, we have developed a tensor network ansatz for the Loop-String-Hadron formulation [38], whereby one can calculate static and dynamic properties of this theory. We will skip the details of the implementations and briefly explain the essentials to establish the workflow. The ansatz is defined for the full LSH Hamiltonian given in Eq. 13. Accordingly, all subsequent definitions of the Hilbert space and the associated operators are formulated with respect to the full theory. The full Hilbert space at each site is characterized by a set of three quantum numbers $|n_l, n_i, n_o\rangle$ and the MPS ansatz is directly endowed with this structure. Formally, one can write it down as follows:

$$|\Psi[A]\rangle = \sum_{p_1, \dots, p_N} A_{p_1}^{a_1} A_{p_2}^{a_1, a_2} \dots A_{p_N}^{a_{N-1}} |p_1, p_2, \dots, p_N\rangle. \quad (45)$$

Here, p_r corresponds to the physical states at each lattice site r . The notation $|p_1, p_2, \dots, p_N\rangle \equiv \otimes_{r=1}^N |p_r\rangle$, where $|p\rangle_r \equiv |n_l, n_i, n_o\rangle_r$. The variational degrees of freedom are contained in the A -matrices, which is defined at each sites and populated by complex entries. We further impose the two global symmetries of the LSH Hamiltonian, namely \mathcal{B} and q into the local tensor structure to yield a blocksparse representation. We rely on the ITensors.jl library [56, 57] and its inbuilt functions to construct the MPS/MPO functions. For time-evolving the initial state, we use the 2-site TDVP algorithm [58] defined in the library. Due to computational overhead with the 2-site algorithm, we have opted to keep the maximum bond-dimension to 200. This will result in errors accumulating as the time evolution progresses, and is reflected in the entanglement entropy plot in Fig. 4. Tabulated values this error is presented in the Supplementary information. The simulation is set up for each value of $x \in \{50, 100, 200\}$ by first initializing two product state MPSes, one for the strong-coupling vacuum state and the other for the string-configurations. Both of these states correspond to the same symmetry sector of the LSH Hamiltonian and the algorithm trivially conserves these quantum numbers by construction. The relevant observables are computed for both these time evolved states and subtract to isolate the evolution of the initialized meson.

Benchmarking via PPM

We benchmark quantum processing unit (QPU) observables using the Pauli Propagation Method (PPM), a Heisenberg-picture simulator that back-propagates the measured observable O through the circuit partitioned into logical layers. Under Clifford evolution, Pauli operators map to Pauli operators; consequently, purely Clifford layers preserve the operator's Pauli support and do not increase the number of qubit-wise non-commuting terms. By contrast, a non-Clifford layer whose generator anticommutes with a Pauli component of O can induce branching: in the worst

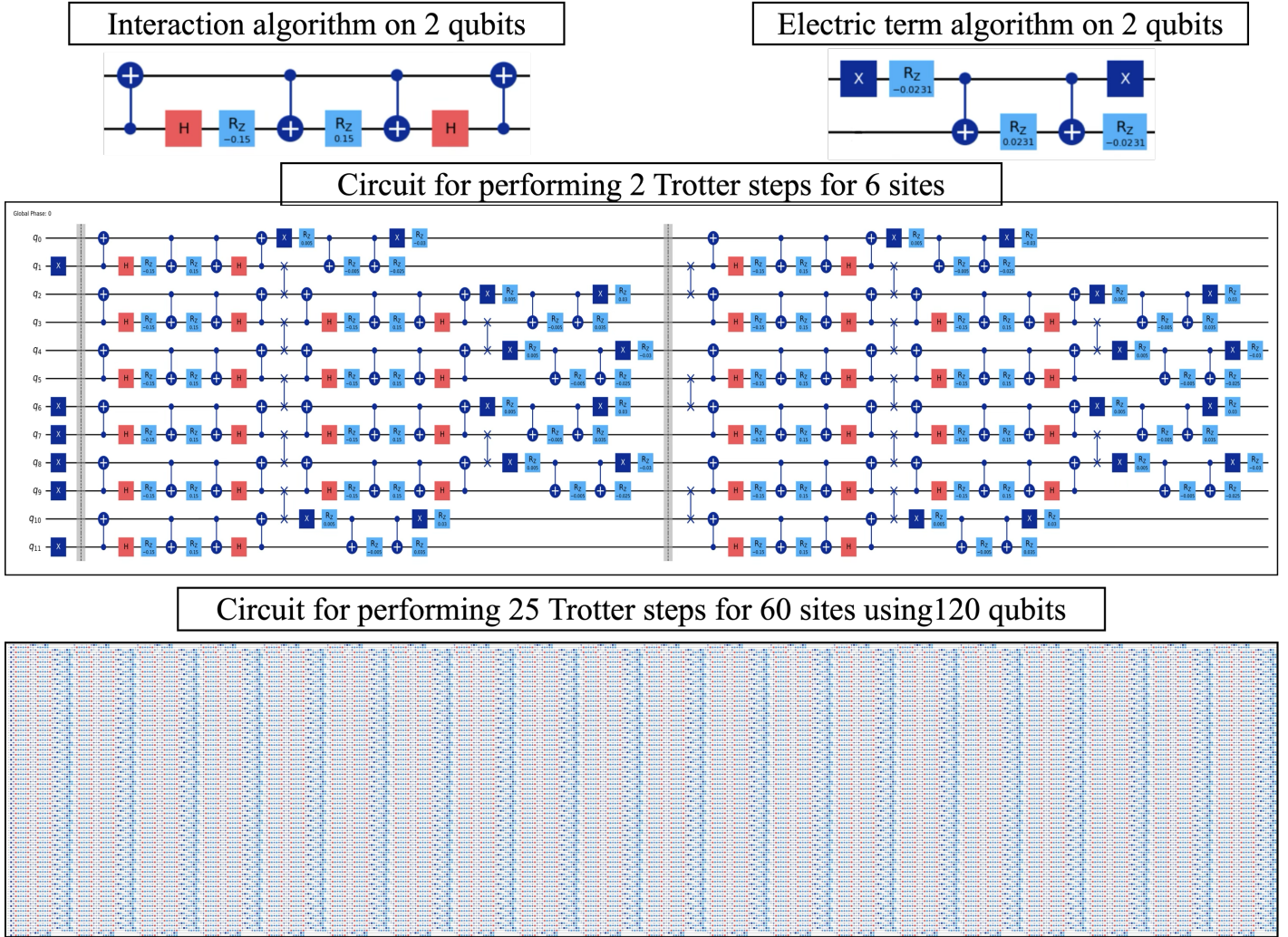


Fig. 6: The Quantum Circuit: implements unitaries constructed for each term of the Hamiltonian. The mass Hamiltonian is a single qubit rotation, while the building block of electric term and interaction term of the Hamiltonian are 2-qubit operations. Use of a number of swap gates allows simultaneous application of the unitaries for both in a single Trotter step. The middle panel presents two Trotter steps of the full algorithm over 6 lattice sites, initialized with a pair of hadron-antihadron at the center. The bottom panel presents the quantum circuit employed in this study with 25 Trotter steps of the full algorithm over 60 lattice sites for $x = 100$, initialized with a meson at the center. The full circuit consists of 17660 2-qubit gates and over 60000 single-qubit gates.

case, the number of Pauli terms doubles across such a layer, leading to exponential growth in the term count with circuit depth. To bound the computational cost, one may truncate by discarding Pauli terms whose coefficients fall below a prescribed threshold during back-propagation, trading accuracy for tractability in a controlled manner.

In this work, we target non-truncated PPM, i.e., back-propagation proceeds without discarding terms, rendering the result effectively exact up to floating-point tolerances. Since there is no immediate way to identify the number of Pauli terms required to backpropagate the circuit completely and exactly, to set a safe compute budget, we empirically upper-bounded the Pauli-term cardinality at the circuit input as follows: we tracked (i) the number of Pauli terms and (ii) the remaining layer depth over an initial segment of the back-propagation, then extrapolated to depth zero. The inferred terminal term counts were 9,400, 12,500, and 66,000 for $x = 50, 100$ and 200 , respectively. Within these budgets, back-propagation is *expected* to be completed without, or minor, truncation. Accordingly, the PPM estimates serve as reference values for the corresponding QPU observables at these settings and scales.

End Notes

In Fig. 4, we provide a quantitative comparison of the benchmarks for three different values of x . It is found that as the system approaches the weak-coupling or continuum limit, the quantum processor maintains structural robustness where classical tensor networks and Pauli propagation methods encounter the growth of entanglement, and magic beyond the capacity of a fixed classical computing hardware and classical algorithm. This leads to a loss of physical information about the system reflected in drop of entanglement entropy or symmetry violations even with classical hardware. Quantum processor maintains structural robustness as reflected in: 1) 2) 3) Violation of global symmetry is very small, as you find from the reference lines in the middle row. Microscopically, violation in QPU is of the same order as in PP for $x=200$. However, for PP, the violation increases steadily as t increases, whereas there is no such trend in the QPU performance.

- maintaining a lightcone to emerge as an outcome of the differential measurement for all values of x . This is pretty nontrivial given the scale of the circuit (see Fig. 6) it implements.
- A careful look at the top-most panel of Fig. 4 shows that the oscillation in the number density is captured by the QPU for all cases, whereas MPS clearly fails for $x = 200$ as it hits the entanglement wall demonstrated in the bottom row the same figure.
- Violation of global symmetry is very small (middle panel of Fig. 4), as evident from the reference lines in the middle row. For $x = 50$, the PP simulates the classical circuit without any error and it preserves the global symmetries accurately. PP starts to violate the symmetries for a longer time scale and for a larger value of x . Microscopically, violation in QPU due to hardware noise is of the same order as in PP when it exists. However, for PP, the violation increases steadily with t , whereas there is no such trend in QPU performance.

These observations support the possibility of robust quantum simulation of non-Abelian gauge theory and would yield a potential benefit once hardware noise subsides.

Data Availability

The data supporting the findings of this study are available at the public [GitHub](#) repository.

Code Availability

The codes used for the findings of this study are available from the corresponding author upon reasonable request.

Acknowledgments

The authors would like to thank Abhinav Kandala for insightful discussions and feedback at various points of this work and for sharing comments on the manuscript. IR would like to thank Jesse Stryker, Zohreh Davoudi, Saurabh Kadam, Navya Gupta, and Aahiri Naskar for their contribution to developing the loop-string-hadron framework and numerous discussions during all collaboration meetings. The work reported here is performed using the IBM Quantum Credits received by IR. The authors acknowledge the support. IR acknowledges useful discussions during meetings of QC4HEP working group. Research of IR is supported by the OPERA award (FR/SCM/11-Dec-2020/PHY) from BITS-Pilani and the cross-discipline research fund (C1/23/185) from BITS-Pilani. FI is supported by the cross-discipline research fund (C1/23/185) from BITS-Pilani, received by IR.

Authors' contributions

FI developed the quantum algorithm and benchmarked it against exact diagonalization, prepared the POC, performed noiseless classical simulation of the quantum algorithm. **RM** helped design and map the quantum circuit tailored to the hardware, and ran all the quantum experiments, and performed noiseless classical simulation of the quantum algorithm. **EM** performed the tensor network calculations to benchmark the performance of QPU, making all the plots and analyzing data. **NE** helped analyze the quantum circuits and experimental results & evaluation, and contributed to manuscript preparation. **IR** developed the problem statement, set up the algorithmic strategy, analysed data, prepared the main manuscript, including graphics.

Competing interests

The authors declare no competing interests.

References

- [1] Martinez, E. A., Muschik, C. A., Schindler, P., Nigg, D., Erhard, A., Heyl, M., Hauke, P., Dalmonde, M., Monz, T., Zoller, P., et al. *Nature* **534**(7608), 516–519 (2016).
- [2] Yang, B., Sun, H., Ott, R., Wang, H.-Y., Zache, T. V., Halimeh, J. C., Yuan, Z.-S., Hauke, P., and Pan, J.-W. *Nature* **587**(7834), 392–396 (2020).
- [3] Mil, A., Zache, T. V., Hegde, A., Xia, A., Bhatt, R. P., Oberthaler, M. K., Hauke, P., Berges, J., and Jendrzejewski, F. *Science* **367**(6482), 1128–1130 (2020).

- [4] Mildenerger, J., Mruczkiewicz, W., Halimeh, J. C., Jiang, Z., and Hauke, P. *Nature Physics* **21**(2), 312–317 (2025).
- [5] Meth, M., Zhang, J., Haase, J. F., Edmunds, C., Postler, L., Jena, A. J., Steiner, A., Dellantonio, L., Blatt, R., Zoller, P., et al. *Nature Physics*, 1–7 (2025).
- [6] Cochran, T. A., Jobst, B., Rosenberg, E., Lensky, Y. D., Gyawali, G., Eassa, N., Will, M., Szasz, A., Abanin, D., Acharya, R., et al. *Nature*, 1–6 (2025).
- [7] Zhou, Z.-Y., Su, G.-X., Halimeh, J. C., Ott, R., Sun, H., Hauke, P., Yang, B., Yuan, Z.-S., Berges, J., and Pan, J.-W. *Science* **377**(6603), 311–314 (2022).
- [8] Mueller, N., Wang, T., Katz, O., Davoudi, Z., and Cetina, M. *Nature Communications* **16**(1), 5492 (2025).
- [9] Schweizer, C., Grusdt, F., Berngruber, M., Barbiero, L., Demler, E., Goldman, N., Bloch, I., and Aidelsburger, M. *Nature Physics* **15**(11), 1168–1173 (2019).
- [10] Mueller, N., Carolan, J. A., Connelly, A., Davoudi, Z., Dumitrescu, E. F., and Yeter-Aydeniz, K. *PRX Quantum* **4**(3), 030323 (2023).
- [11] Farrell, R. C., Illa, M., Ciavarella, A. N., and Savage, M. J. *Physical Review D* **109**(11), 114510 (2024).
- [12] Davoudi, Z., Hsieh, C.-C., and Kadam, S. V. *Quantum* **8**, 1520 (2024).
- [13] Cobos, J., Fraxanet, J., Benito, C., di Marcantonio, F., Rivero, P., Kapás, K., Werner, M. A., Legeza, Ö., Bermudez, A., and Rico, E. *arXiv preprint arXiv:2507.08088* (2025).
- [14] Klco, N., Savage, M. J., and Stryker, J. R. *Physical Review D* **101**(7), 074512 (2020).
- [15] Ciavarella, A., Klco, N., and Savage, M. J. *Physical Review D* **103**(9), 094501 (2021).
- [16] Atas, Y. Y., Zhang, J., Lewis, R., Jahanpour, A., Haase, J. F., and Muschik, C. A. *Nature communications* **12**(1), 6499 (2021).
- [17] Atas, Y. Y., Haase, J. F., Zhang, J., Wei, V., Pfaendler, S. M.-L., Lewis, R., and Muschik, C. A. *Physical Review Research* **5**(3), 033184 (2023).
- [18] Ciavarella, A. N. and Bauer, C. W. *Physical Review Letters* **133**(11), 111901 (2024).
- [19] Bauer, C. W., Davoudi, Z., Klco, N., and Savage, M. J. *Nature Reviews Physics* **5**(7), 420–432 (2023).
- [20] Di Meglio, A., Jansen, K., Tavernelli, I., Alexandrou, C., Arunachalam, S., Bauer, C. W., Borrás, K., Carrazza, S., Crippa, A., Croft, V., et al. *PRX quantum* **5**(3), 037001 (2024).
- [21] Raychowdhury, I. and Stryker, J. R. *Physical Review D* **101**, 114502 (2020).
- [22] Van Den Berg, E., Mineev, Z. K., and Temme, K. *Physical Review A* **105**(3), 032620 (2022).
- [23] Rudolph, M. S., Jones, T., Teng, Y., Angrisani, A., and Holmes, Z. *arXiv preprint arXiv:2505.21606* (2025).
- [24] Amorosso, R., Syritysyn, S., and Venugopalan, R. *Physics Letters B* **868**, 139806 (2025).
- [25] Altmann, J., Dubla, A., Greco, V., Rossi, A., and Skands, P. *The European Physical Journal C* **85**(1), 16 (2025).
- [26] Müller, B. and Schäfer, A. 11 (2022).
- [27] Kogut, J. and Susskind, L. *Physical Review D* **11**, 395 (1975).
- [28] Hamer, C., Oitmaa, J., and Weihong, Z. *Physical Review D* **45**(12), 4652 (1992).
- [29] Kim, Y., Eddins, A., Anand, S., Wei, K. X., Van Den Berg, E., Rosenblatt, S., Nayfeh, H., Wu, Y., Zaletel, M., Temme, K., et al. *Nature* **618**(7965), 500–505 (2023).
- [30] Mathur, M. *Journal of Physics A: Mathematical and General* **38**(46), 10015 (2005).
- [31] Mathur, M. *Nuclear Physics B* **779**(1-2), 32–62 (2007).
- [32] Anishetty, R. and Raychowdhury, I. *arXiv preprint arXiv:1408.6331* (2014).
- [33] Raychowdhury, I. *The European Physical Journal C* **79**(3), 235 (2019).
- [34] Davoudi, Z., Shaw, A. F., and Stryker, J. R. *Quantum* **7**, 1213 (2023).
- [35] Dasgupta, R. and Raychowdhury, I. *Physical Review A* **105**(2), 023322 (2022).
- [36] Mueller, B. and Schaefer, A. *International Journal of Modern Physics E* **20**(11), 2235–2267 (2011).
- [37] Ebner, L., Müller, B., Schäfer, A., Schmotzer, L., Seidl, C., and Yao, X. *Communications Physics* **8**(1), 368 (2025).
- [38] Mathew, E., Gupta, N., V. Kadam, S., Bapat, A., Stryker, J., Davoudi, Z., and Raychowdhury, I. *PoS LATTICE2024*, 472 (2025).
- [39] Raychowdhury, I. *Prepotential Formulation of Lattice Gauge Theories*. PhD thesis, Calcutta U., (2013).
- [40] Kadam, S. V., Raychowdhury, I., and Stryker, J. R. *Phys. Rev. D* **107**, 094513 May (2023).
- [41] Kadam, S. V., Naskar, A., Raychowdhury, I., and Stryker, J. R. *Phys. Rev. D* **111**, 074516 Apr (2025).
- [42] Kadam, S. V., Naskar, A., Raychowdhury, I., and Stryker, J. R. (2025).
- [43] Lanes, O., Beji, M., Corcoles, A. D., Dalyac, C., Gambetta, J. M., Henriot, L., Javadi-Abhari, A., Kandala, A., Mezzacapo, A., Porter, C., Sheldon, S., Watrous, J., Zoufal, C., Dauphin, A., and Peropadre, B. (2025).
- [44] Mathur, M. *J. Phys. A* **38**, 10015–10026 (2005).
- [45] Mathur, M. *Nucl. Phys. B* **779**, 32–62 (2007).
- [46] Mathur, M., Raychowdhury, I., and Anishetty, R. *J. Math. Phys.* **51**, 093504 (2010).
- [47] Anishetty, R., Mathur, M., and Raychowdhury, I. *J. Math. Phys.* **50**, 053503 (2009).
- [48] Anishetty, R., Mathur, M., and Raychowdhury, I. *J. Phys. A* **43**, 035403 (2010).
- [49] Anishetty, R. and Raychowdhury, I. *Phys. Rev. D* **90**(11), 114503 (2014).
- [50] Raychowdhury, I. and Anishetty, R. *PoS LATTICE2014*, 313 (2014).
- [51] Raychowdhury, I. *Eur. Phys. J. C* **79**(3), 235 (2019).
- [52] Davoudi, Z., Raychowdhury, I., and Shaw, A. *Physical Review D* **104**(7), 074505 (2021).
- [53] Schollwoeck, U. *Annals Phys.* **326**, 96–192 (2011).
- [54] Bañuls, M. C. *Ann. Rev. Condensed Matter Phys.* **14**, 173–191 (2023).
- [55] Bañuls, M. C. and Cichy, K. *Rept. Prog. Phys.* **83**(2), 024401 (2020).

- [56] Fishman, M., White, S. R., and Stoudenmire, E. M. *SciPost Phys. Codebases* , 4 (2022).
- [57] Fishman, M., White, S. R., and Stoudenmire, E. M. *SciPost Phys. Codebases* , 4–r0.3 (2022).
- [58] Paeckel, S., Köhler, T., Swoboda, A., Manmana, S. R., Schollwöck, U., and Hubig, C. *Annals Phys.* **411**, 167998 (2019).

Supplementary Information

Quantum simulation vs. classical simulation

Here we present a comparison of heatmaps obtained via tensor network simulation for the full theory. The robustness of QPU performance is evident in the consistently increasing width of the lightcone as x increases, which is consistent with the classical simulation as well. Fig. 11 shows the QPU results for 25 Trotter steps. It is clear that noise dominates at later times as the 2-qubit gate depth increases to 324 at the 25th step. The signal still appears coherent, while the contrast decays with time. However, once studied for the same physical time, for different values of the coupling x , the QPU output remains robust as shown in Fig. 7.

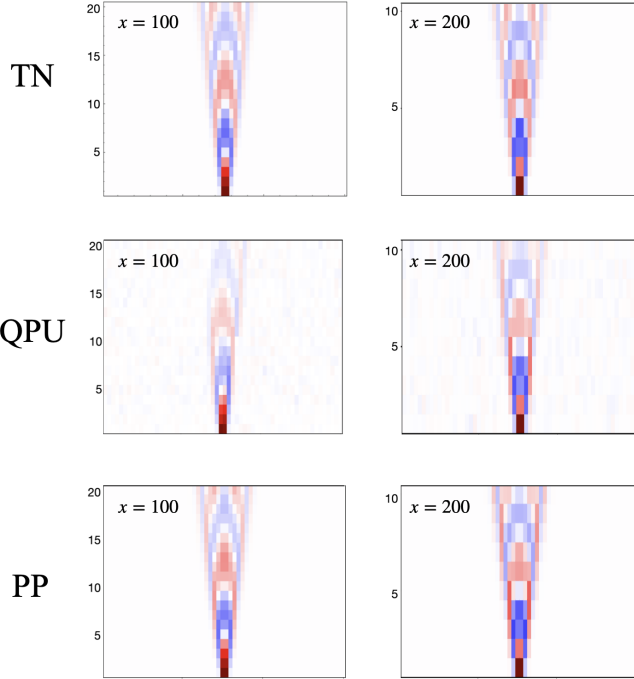


Fig. 7: Comparing dynamics for the same physical time for $x=100$ and $x=200$

The compute time for MPS calculation is presented in Fig. 8 and the same for PP is presented in Fig. 10.

The estimated error in the tensor network calculation is directly related to the errors building up as the time evolution progresses due to finite bond dimension. This error corresponds to the sum of the Schmidt values that were discarded after each time step as tabulated in Table 1.

A relative deviation for the data points between MPS, PP and QPU is presented in 9

measurement protocol and error mitigation strategy

The output from the QPU is presented here with only measurement-error mitigation (TRES). This is decided based on comparing the outcome of simulated noise with the ideal result for a system of 24 qubits as shown in Fig. 12.

One major reason to obtain reasonably good result only with measurement error mitigation is due to the differential measurement protocol being employed in this work. This protocol not

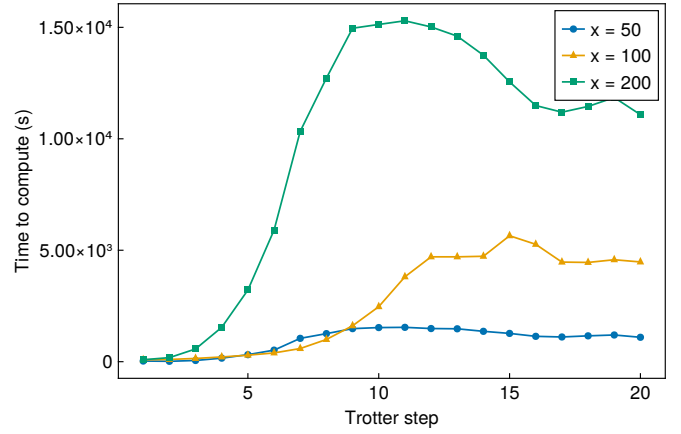


Fig. 8: Clock time for computing each Trotter step of the TN calculation on a Mac Pro tower (3.2GHz 16-core 4.4GHz Intel Xeon W processor, 96GB).

Trotter step	Truncation Error		
	$x = 200$	$x = 100$	$x = 50$
1	10^{-11}	10^{-11}	10^{-11}
2	10^{-11}	10^{-11}	10^{-11}
3	10^{-11}	10^{-11}	10^{-11}
4	10^{-11}	10^{-11}	10^{-11}
5	10^{-11}	10^{-11}	10^{-11}
6	10^{-9}	10^{-11}	10^{-11}
7	10^{-7}	10^{-11}	10^{-11}
8	10^{-6}	10^{-11}	10^{-11}
9	10^{-4}	10^{-11}	10^{-11}
10	10^{-3}	10^{-11}	10^{-11}
11	10^{-3}	10^{-10}	10^{-11}
12	10^{-3}	10^{-9}	10^{-11}
13	10^{-2}	10^{-8}	10^{-11}
14	10^{-2}	10^{-7}	10^{-11}
15	10^{-2}	10^{-6}	10^{-11}
16	10^{-3}	10^{-5}	10^{-11}
17	10^{-3}	10^{-5}	10^{-11}
18	10^{-3}	10^{-4}	10^{-11}
19	10^{-3}	10^{-4}	10^{-11}
20	10^{-3}	10^{-4}	10^{-11}

Table 1: The maximum truncation error in the Schmidt values for the time evolved state at each TDVP time step

only cancels any bias present in the hardware result, but also completely diminishes any boundary effect present in the calculation. As the hadron spreads, performing calculation with a large lattice becomes more and more crucial to avoid any boundary effect. This is represented in Fig. 13.

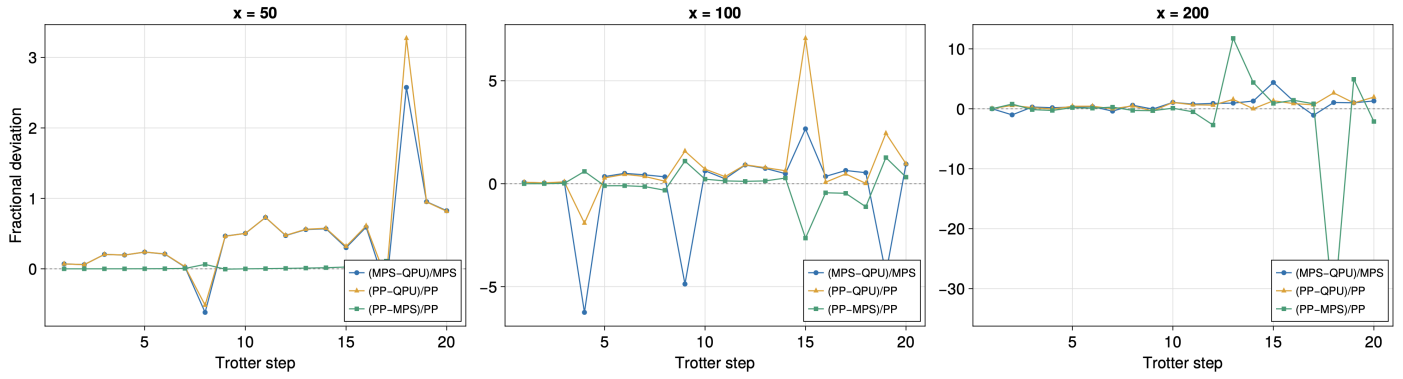


Fig. 9: Relative deviation of data sets obtained with MPS, PP and QPU are compared for $x=50,100,200$.

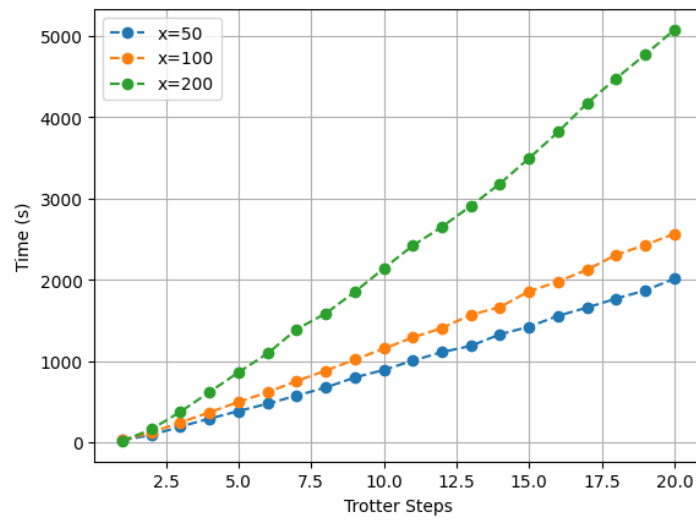


Fig. 10: Compute time for Pauli propagation using HP Z2 Tower G9 Workstation. The maximum number of allowed term is chosen to be different for different values of x , as per linear estimate from small size exact results.

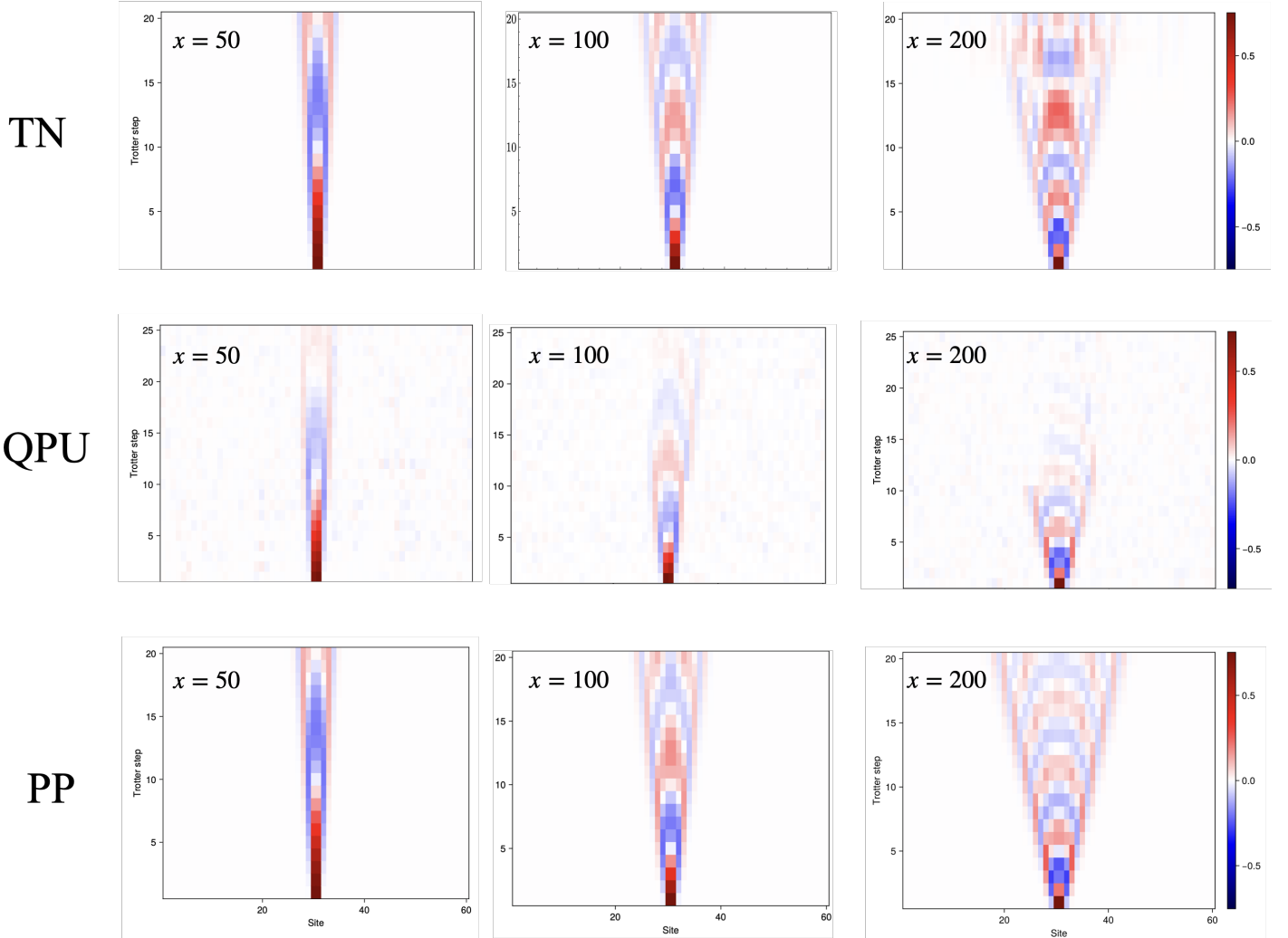


Fig. 11: The quantum simulation protocol is further tested for a couple of different values of coupling $x = 50$ and $x = 200$, without changing the value of m/g . The experimental observation for 25 Trotter steps, given in the middle row confirms the expected ‘shrinking’ and ‘widening’ of light cone structure in Hadron propagation respectively apart from noise being dominant over later time-steps as x increases. The top panel shows the result obtained via tensor network calculations for upto 20 Trotter steps. For $x = 100$, The TN calculation breaks down beyond 20 Trotter steps for $x = 100$ (not shown in the figure), while the same for $x = 200$ is manifest in the top right plot. The Pauli propagation result for all three values of x provides the simulated noiseless outcome from QPU with proper estimation of maximum number of terms to consider as obtained by extrapolating exact number for the same for initial few time slices. The mismatch between Pauli propagation result and tensor network result allows one to identify when the later method breaks down (evident for $x = 200$, $N_\tau > 10$). However, these quantum simulations are performed keeping the size of Trotter steps to be the same, and hence following (31) and (32), the time evolution for a fixed time t is achieved by N_τ to be 40, 20, 10 for the value of x to be 50, 100, 200 respectively.

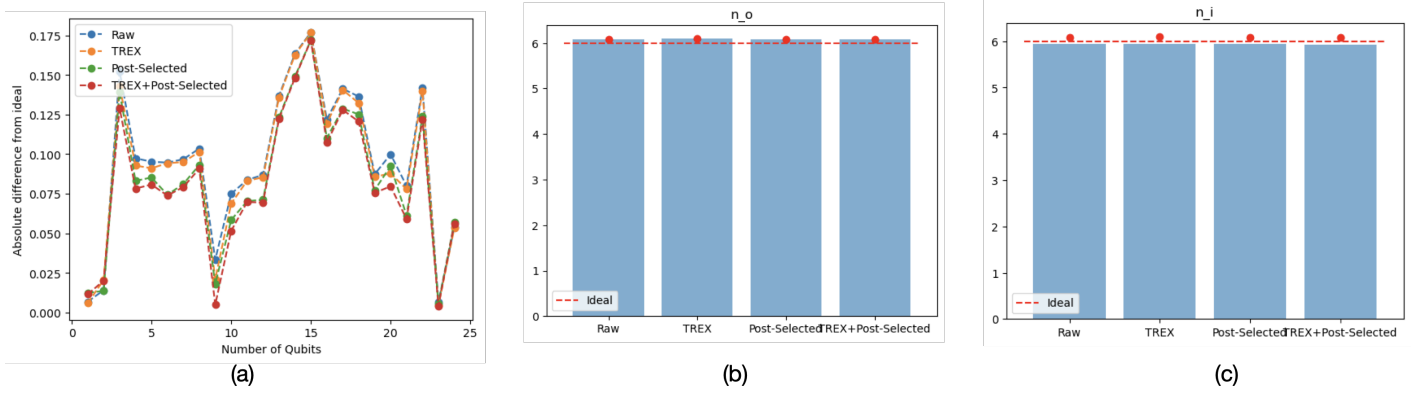


Fig. 12: POC for error mitigation strategy employed: for a small scale system of 24 qubits, ideal noiseless result is obtained by classical simulation. Noisy simulation for the same is also obtained. (a) Absolute difference from ideal result for raw, measurement error mitigation (TREX), post selection and using both are compared. It appears that TREX alone is being able to provide good result. (b), (c) Globally conserved charges stay robust with all the methods.

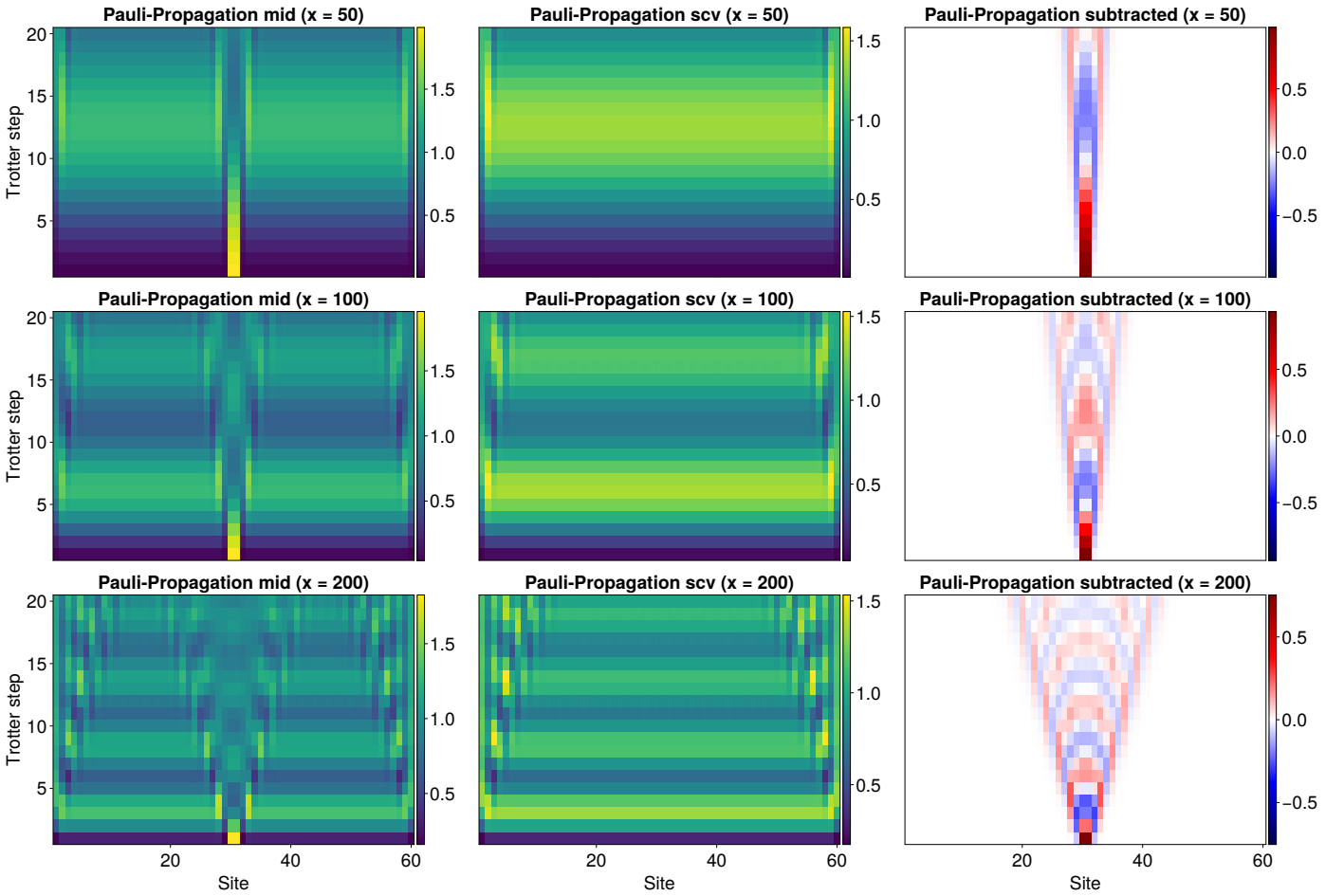


Fig. 13: Demonstrating differential measurement protocol for PP. The leftmost column represents propagation of hadron, placed at the center of the finite size lattice for theories with coupling constant $x = 50, 100, 200$. The middle column represents dynamical evolution of the SCV for all three cases. The rightmost column represents the difference between the first two column, which is presented as the result in this current work. It is evident that boundary effects dominate for larger value of x , and hence working with a large lattice is crucial to approach $x \rightarrow \infty$ limit. While this demonstration is with the simulation of noiseless circuit, for the experimental measurement on noisy hardware, some systematic error, mostly if any bias is present gets cancelled and in effect high fidelity results are obtained without active error mitigation.